Enhanced superconductivity in SrTiO₃-based interfaces via amorphous Al₂O₃ capping

I. Silber ☉,[1] A. Azulay ☉,[2] A. Basha ☉,[2] D. Ketchker ☉,[1] M. Baskin,[3] A. Yagoda,[1] L. Kornblum,[3] A. Kohn ☉,[2] and Y. Dagan ☉[1]

[1]*School of Physics and Astronomy, Tel Aviv University, Tel Aviv 69978, Israel*

[2]*Department of Materials Science and Engineering, The Iby and Aladar Fleischman Faculty of Engineering, Tel Aviv University, Tel Aviv 6997801, Israel*

[3]*The Andrew and Erna Viterbi Faculty of Electrical and Computer Engineering, Technion – Israel Institute of Technology, Haifa 32000-03, Israel*

Oxide interfaces feature unique two-dimensional (2D) electronic systems with diverse electronic properties such as tunable spin-orbit interaction and superconductivity. Conductivity emerges in these interfaces when the thickness of an epitaxial polar layer surpasses a critical value, leading to charge transfer to the interface. Here, we show that depositing amorphous Al_2O_3 on top of the polar oxide can reduce the critical thickness and enhance the superconducting properties for $SrTiO_3$-based interfaces. A detailed transmission electron microscopy analysis reveals that the enhancement of the superconducting properties is linked to the expansion of the $SrTiO_3$ lattice in a direction perpendicular to the interface. We propose that the increase in the superconducting critical temperature, T_c, is a result of epitaxial strain.

I. INTRODUCTION

The phenomenon of superconductivity in semiconductors with an extremely low electron density remains a puzzle. The mystery lies in how these electrons, characterized by a substantial Coulomb repulsion and a limited density of states, can condense into a superconducting ground state. A hallmark example is doped $SrTiO_3$ [1], which superconducts at very low carrier densities ($n \approx 6 \times 10^{17}$ cm^{-3}, one electron per 30 000 unit cells) [2], and its superconducting mechanism is under debate [3–6]. Moreover, the carrier-temperature phase diagram shows superconductivity in a dome-shaped region [7–10]. This unusual behavior has also been observed in $SrTiO_3$-based interfaces [11,12]. However, the superconducting transition temperature T_c in interfaces has always been smaller than the bulk counterpart [13,14].

Interfacial conductivity can occur when a layer of a polar oxide, such as $LaAlO_3$ ($a = 0.379$ nm [15]), is epitaxially deposited on an undoped $SrTiO_3$ ($a = 0.3905$ nm [16]). When the polar layer surpasses a specific thickness, conductivity emerges [17]. The electron system is limited to a few unit cells near the interface [18–20]. The straightforward explanation for the observed criticality in polar-layer thickness is the necessity for a large enough electric field to initiate charge transfer to the interface [21–23]. This critical thickness can be reduced by depositing a metallic [24–26] or another oxide [27,28] layer on top of the polar oxide (capping). However, the decrease of the critical thickness usually does not improve the superconducting properties compared with the uncapped $LaAlO_3/SrTiO_3$ interface.

Here we show that by deposition of an amorphous Al_2O_3 capping layer on top of an ultrathin epitaxial $LaAlO_3$, the (111) $Al_2O_3/LaAlO_3/SrTiO_3$ interface becomes conducting and superconducting with $T_c = 420$ mK, which is about 20% higher than the uncapped interface.

Strain analysis using high-angle annular dark-field scanning transmission electron microscopy (HAADF STEM) images shows that the interfacial $SrTiO_3$ layers expand perpendicular to the interface by up to $1.3\% \pm 0.6\%$ with respect to $SrTiO_3$ regions away from the interface. Conversely, the strain in the interfacial $SrTiO_3$ for an uncapped sample with a thicker $LaAlO_3$ layer is within the uncertainty range, and its $LaAlO_3$ lattice parameter contracts by up to $4.5\% \pm 1\%$. We correlate T_c with the lattice expansion, proposing that the observed enhancement of the superconducting critical temperature is due to the strain exerted by the $LaAlO_3$ layer on the topmost $SrTiO_3$ layers, where conductivity and superconductivity reside.

II. SAMPLE DESIGN AND STRUCTURAL ANALYSIS

We fabricated a series of $Al_2O_3/LaAlO_3/SrTiO_3$ samples with a constant amorphous Al_2O_3 thickness of 10 nm and varying $LaAlO_3$ thickness in the [111] direction of the $SrTiO_3$ substrate (see Table S1 in the Supplemental Material [29]). We deliberately employed deposition conditions to prevent surface reduction of $SrTiO_3$. The $LaAlO_3$ thickness is measured in monolayers (ML) consisting of one layer of LaO_3 and one layer of Al. We designate the various samples by specifying the number of monolayers, and samples without Al_2O_3 are denoted as uncapped.

Figure 1(a) shows a cross-sectional high-angle dark-field scanning transmission electron microscope image of the 3 ML sample, revealing an STO[111][1$\bar{1}$0] ∥ LAO[111][1$\bar{1}$0] epitaxial relation, as expected (see Fig. S3 [29]). The highlighted peaks in the power spectrum (inset) are attributed to reciprocal-lattice vectors $g_{1\bar{1}0}$ and g_{111}, namely interplanar spacings of $d_{110} \sim 0.276$ nm and $d_{111} \sim 0.225$ nm, respectively, in STO of the $Pm\bar{3}m$ space group.

Elemental maps obtained by energy-dispersive x-ray spectroscopy (EDS), representing net intensities of Sr *L*, Ti *K*, La
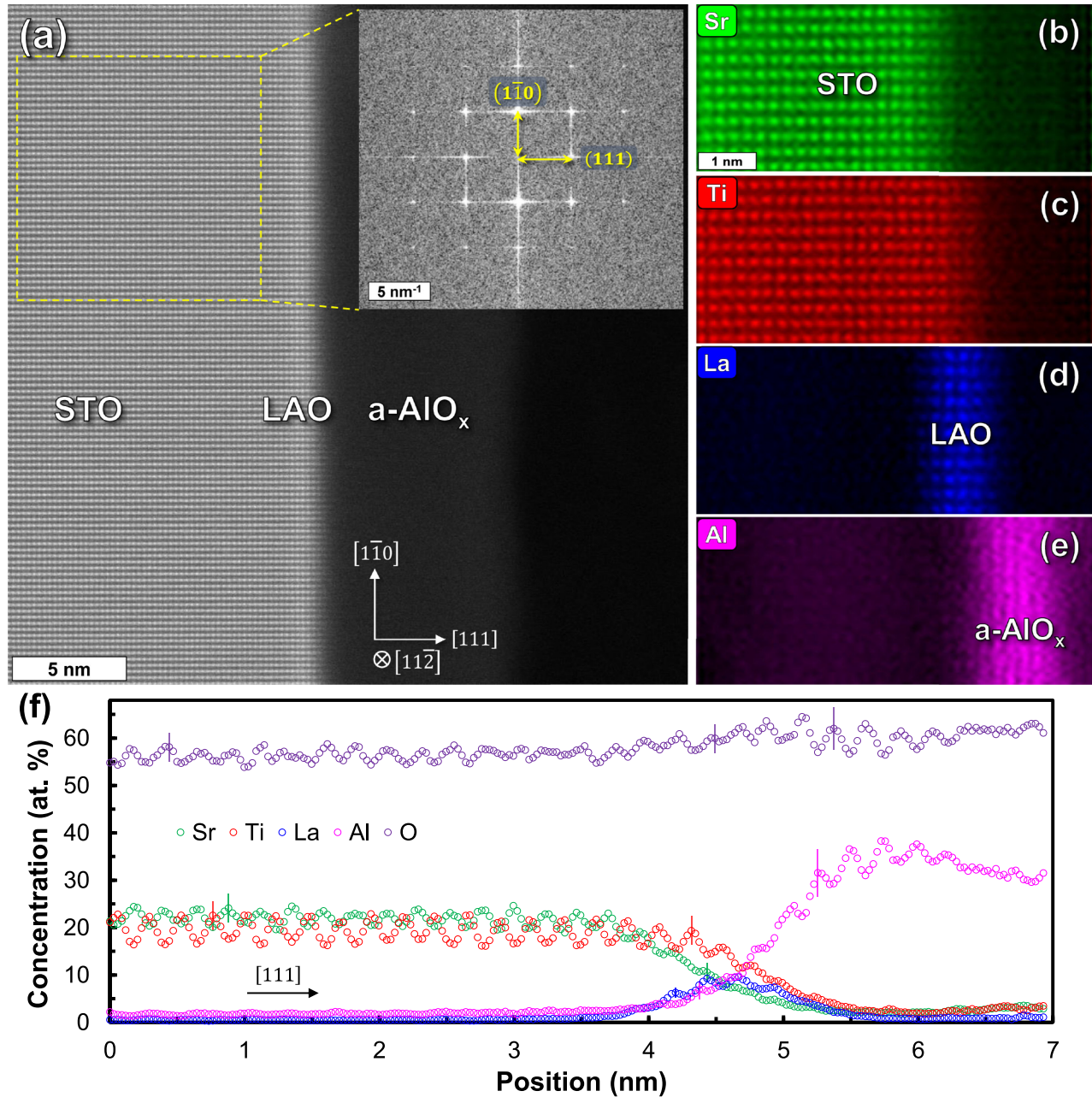
FIG. 1. Structure and composition of the 3 ML capped sample. (a) Cross-sectional high-angle annular dark-field scanning transmission electron microscope image showing atomic-column resolution of the sample comprising three $LaAlO_3$ monolayers covered by amorphous alumina, grown on a $SrTiO_3$ (111) substrate and oriented to the $[11\bar{2}]$ zone axis. The inset shows the power spectrum calculated from the region marked by the yellow square. (b)–(e) Elemental maps obtained by energy-dispersive x-ray spectroscopy (EDS) using net intensities of Sr *L*, Ti *K*, La *L*, and Al *K* characteristic x-ray photon energies. (f) Concentrations of Sr, Ti, La, and Al along the [111] direction, obtained by integration over the width of the images shown in (b)–(e) followed by Cliff-Lorimer *k*-factor quantification. Error bars represent typical compositional uncertainty in that region.

L, and Al *K* characteristic x-ray photon energies, are shown in Figs. 1(b)–1(e). These maps reveal Sr, Ti, La, and Al atomic columns viewed along the $[11\bar{2}]$ zone axis, e.g., Sr and Ti alternating at (111) planes, as expected from our design of the $Al_2O_3/LaAlO_3/SrTiO_3$ structure. Integration of the signal over the width of the images shown in Figs. 1(b)–1(e) followed by elemental quantification is presented in Fig. 1(f). The oscillating peaks of Sr and Ti concentration suggest that the Sr to Ti atomic ratio is ~1 in the $SrTiO_3$ region.

However, the gradual decrease in Sr content through the $LaAlO_3$ region indicates partial substitution of Sr for La, as observed previously [30,31]. Furthermore, for the amorphous Al_2O_3 region, around a 2:3 Al:O atomic ratio is observed. Similar results are obtained for the uncapped 14 ML sample; see Fig. S4 [29]. We note that the oscillating peaks of Al concentration in the amorphous Al_2O_3 region may stem from partial crystallization due to exposure to the electron beam during EDS acquisition [32]. Also, we note that the minor
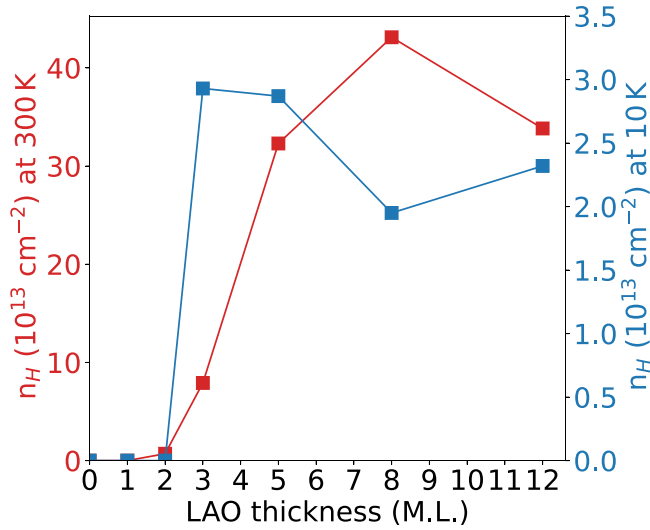
FIG. 2. Reduced critical thickness of (111) $Al_2O_3/LaAlO_3/$ $SrTiO_3$ interface. The measured Hall number at 300 and 10 K, as a function of the $LaAlO_3$ thickness. The $LaAlO_3$ thickness controls whether the sample is insulating, metallic, or superconducting.

La and Al concentrations observed in the STO region are statistically insignificant (see Fig. S5 [29]). Finally, we note that the deposition of amorphous Al_2O_3 does not effect the structure of the $LaAlO_3/SrTiO_3$ interface as characterized by the TEM analysis (see the Supplemental Material [29]).

III. RESULTS

A. Reduced critical thickness

In uncapped (111)-oriented $LaAlO_3/SrTiO_3$ interfaces, the critical thickness for conductivity is 9 ML [33]. However, adding an Al_2O_3 capping layer decreases the critical thickness for conductivity to 3 ML. This effect can be clearly seen in the Hall number shown in Fig. 2, where measurable carrier density appears only above 2 ML. The variation of the Hall number with temperature is similar to previous studies [34].

We stress again that the $Al_2O_3/SrTiO_3$ interface, without any $LaAlO_3$ layers, is not conducting under our deposition parameters. The few $LaAlO_3$ layers are probably needed to induce a strong enough dipole moment on the surface of the $SrTiO_3$ as suggested in Ref. [23]. Our results showing a reduction of the critical thickness in $Al_2O_3/LaAlO_3/SrTiO_3$ are in accordance with density functional theory calculations that predicted a reduction of the $LaAlO_3$ critical thickness when a neutral layer is added [35].

B. Enhanced superconductivity

Surprisingly, the sample with the critical $LaAlO_3$ thickness of 3 ML has an enhanced superconducting T_c, as seen in Fig. 3. This effect starkly contrasts with previous works, in which the reduction of the $LaAlO_3$ critical thickness resulted in similar or poorer superconducting properties relative to the uncapped interface.

The superconducting state of the Al_2O_3 capped 3 ML sample is two-dimensional in nature as inferred from the different temperature dependence of the critical field for
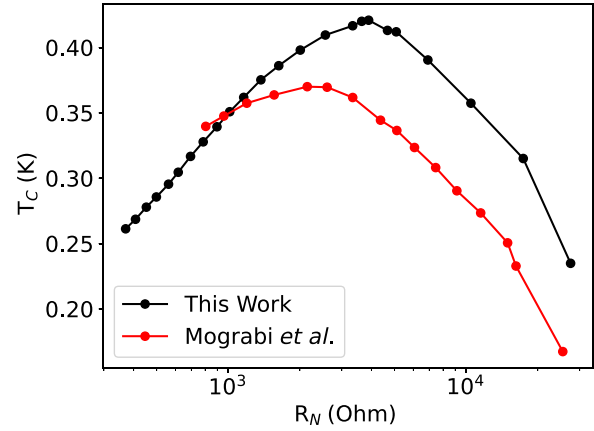

FIG. 3. Enhanced superconductivity with the Al_2O_3 capping for the 3 ML $Al_2O_3/LaAlO_3/SrTiO_3$. The dependence of the superconducting critical temperature vs sheet resistance (controlled by gate voltage) exhibits a dome-shaped line of the phase transition. A significant enhancement of the superconducting critical temperature is observed, compared with a sample without the Al_2O_3 capping (data for the uncapped $LaAlO_3/SrTiO_3$ sample are taken from our previous study [36]).

parallel and perpendicular magnetic field orientations [Fig. 4(b)]. Furthermore, the gate tunability of the conducting and superconducting properties is a characteristic of a two-dimensional conductor [Fig. 4(a)].

From our measurements, we find that $T_c = 420\,\text{mK}$, the Ginzburg-Landau coherence length $\xi_{GL} = 21.4\,\text{nm}$, and the upper bound for the superconducting layer thickness is 10 nm. The lengthscales are comparable to those found in the uncapped $LaAlO_3/SrTiO_3$ interface [37].
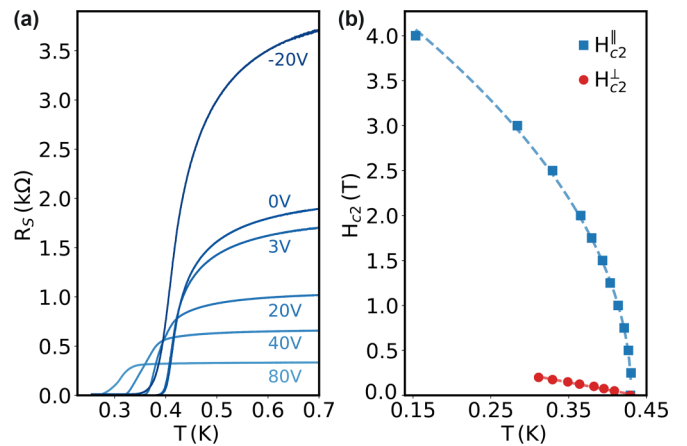

FIG. 4. Superconducting properties of the $Al_2O_3/LaAlO_3/$ $SrTiO_3$ interface for $LaAlO_3$ thickness of 3 ML. (a) The superconducting transition at various back-gate voltages, displaying the nonmonotonic dependence of the transition temperature on the sample normal state resistance. (b) Critical field (zero gate voltage), when the field is applied in-plane or out-of-plane. The characteristic behavior of two-dimensional superconductivity is clearly demonstrated. Dashed lines are fits to the square root for the parallel field configuration and linear for the perpendicular field.
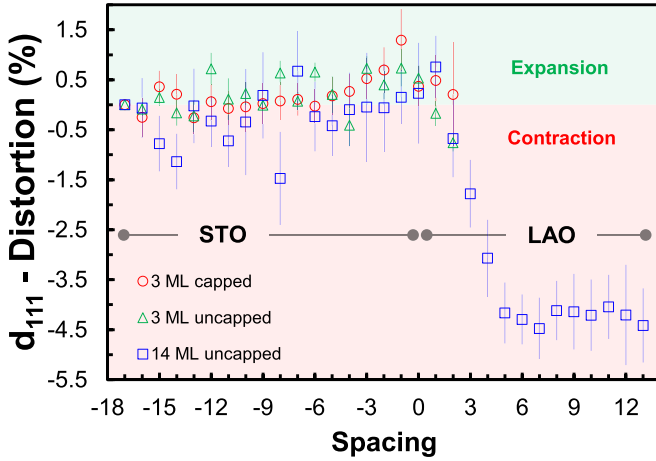
FIG. 5. Detecting strain at the $SrTiO_3$ interface in the 3 ML Al_2O_3/$LaAlO_3$/$SrTiO_3$ sample compared to the uncapped samples. The obtained d_{111} values in the interface region of the Al_2O_3/$LaAlO_3$/$SrTiO_3$ and the two uncapped $LaAlO_3$/$SrTiO_3$ samples were analyzed using five, five, and four high-angle annular dark-field scanning transmission electron microscope images, respectively. The spacing of the $SrTiO_3$ layers away from the interface (no.–18) was used as a reference. Error bars for each spacing represent the standard error of the mean with the corresponding error of the distortion equation.

C. Comparative strain analysis

To elucidate the enhancement of superconducting properties of the 3 ML capped sample compared with the uncapped $LaAlO_3$/$SrTiO_3$ samples, we extract the d_{111} values from HAADF STEM images of the 3 ML capped, as well as 3 and 14 ML uncapped samples.

As shown in Fig. 5, the first three $SrTiO_3$ MLs in the 3 ML capped and uncapped samples expand by up to $1.3\% \pm 0.6\%$ and $0.7\% \pm 0.4\%$, respectively. However, that strain is negligible in the 14 ML uncapped sample, and the $LaAlO_3$ region contracts by up to $4.5\% \pm 1\%$, similar to previous reports [15]. These results suggest that the number of MLs determines the strain exerted on the interfacial $SrTiO_3$, and that this effect is enhanced by the amorphous Al_2O_3 capping.

Along the $[1\bar{1}0]$ direction, strain is unresolvable as the d_{110} values extracted from both $SrTiO_3$ and $LaAlO_3$ regions for all samples are equal, within error (up to 0.6 pm). We also employed the geometric phase analysis (GPA) method to analyze strain, and it corroborated our direct-space analysis detailed above. See Secs. 6 and 7 in the Supplemental Material [29] for further details.

IV. DISCUSSION

In bulk samples of doped $SrTiO_3$, T_c is increased by applying strain, either compressive [38] or tensile [39]. Several mechanisms have been put forth to explain this effect. It has been suggested that compressive strain results in softening of the TO1 optical phonon mode, which is assumed to enhance the superconducting pairing [40], while tensile strain increases ferroelectric fluctuations and again softens the TO1 mode. Even a minute tensile distortion of less than 0.07%, much smaller than what we detect close to the interface in our

samples, modifies the phonon mode substantially and affects the critical temperature [39]. These results were interpreted by evaluating a Grüneisen parameter that diverges with strain, suggesting that the ferroelectric transverse soft phonon mode is dominant in enhancing T_c in $SrTiO_3$ [41].

According to our TEM analysis, using amorphous Al_2O_3 deposition on top of the ultrathin $LaAlO_3$ layer, we have achieved tensile strain in the topmost $SrTiO_3$ layers next to the interface. The amorphous Al_2O_3, in that sense, allows conductivity with a very thin $LaAlO_3$ layer while the $LaAlO_3$ lattice is significantly expanded relative to the relaxed $LaAlO_3$ as we observe in our TEM analysis for the Al_2O_3/$LaAlO_3$/$SrTiO_3$ interface. We phenomenologically correlate the tensile strain and the enhanced superconducting T_c.

Our description is consistent with the fact that the best superconducting properties are observed close to the critical thickness for conductivity. Adding more $LaAlO_3$ layers results in a lower T_c as demonstrated in Table S1 [29]. Based on our analysis, we suggest that this decrease in T_c is due to a smaller $SrTiO_3$ lattice expansion and consequently reduced strain consistent with our proposed origin for the T_c enhancement.

Under our growth conditions, depositing Al_2O_3 directly on $SrTiO_3$ without $LaAlO_3$ is insufficient to generate either conductivity or superconductivity. Ryu *et al.* studied the uncapped (111) $LaAlO_3$/$SrTiO_3$ interface and compared a nonconducting, 3 ML $LaAlO_3$/$SrTiO_3$ sample with a conducting, 20 ML one [34]. They found electronic reconstruction without atomic reconstruction for both interfaces. In addition, the polar structure persists into the $LaAlO_3$ layer. An atomic reconstruction is avoided for both the conducting (20 ML in their case) and the nonconducting (3 ML) sample. We suggest that the absence of atomic reconstruction allowed by the very thin $LaAlO_3$ layer enables the appearance of conductivity in our capped 3 ML interface. Without the $LaAlO_3$ layer, the $SrTiO_3$ surface reconstructs, resulting in a nonpolar interface, which is probably the cause for the lack of conductivity in the $SrTiO_3$/Al_2O_3 interface.

We also note that the data in Fig. 4 suggest that while at 300 K the Hall number increases with $LaAlO_3$ thickness, the number of mobile carriers (inferred from the low-temperature Hall number) at the interface is, in fact, the highest at the critical thickness. However, since the maximum point of the superconducting dome is shifted to higher T_c values, it is not enough to consider the carrier density, which can be tuned for all samples by the gate voltage.

Previous attempts of epitaxial straining of the entire $LaAlO_3$/$SrTiO_3$ interface using different substrates resulted in reduced carrier density [42] and reduced charge mobility [43]. These experiments were performed on (100) interfaces in contrast with our experiment, where the lattice expansion is detected along the [111] direction. It is also possible that the epitaxial strain used in Refs. [42] and [43] resulted in structural defects affecting interfacial conductivity. We have circumvented this problem with our interface design, resulting in an out-of-plane lattice expansion in $SrTiO_3$ along the [111] direction near the interface while maintaining the crystallinity of the heterostructure.

Finally, it is noteworthy that the maximum T_c observed at the critical thickness in (100) capped interfaces is smaller

than that in (111) capped interfaces (365 and 420 mK, respectively). What is the reason for the different T_c? We utilize our findings for the (111) interface and reference the results from Ref. [15] for the (100) interface. While a 3% lattice expansion (relative to relaxed, bulk $LaAlO_3$) is observed for the [111] direction, an order of magnitude smaller expansion of 0.3% is found for the (100) sample. This observation corresponds with our findings of lower T_c in (100) interfaces and further supports our claim that the enhanced superconductivity in (111) Al_2O_3/$LaAlO_3$/$SrTiO_3$ originates from strain.

V. SUMMARY AND CONCLUSION

We show that deposition of amorphous Al_2O_3 on $LaAlO_3$/$SrTiO_3$ interfaces reduces the critical thickness for conductivity to 3 ML. The superconducting T_c is enhanced for the (111) interface at the critical thickness of 3 ML. Structural analysis by STEM leads us to believe that the T_c enhancement in the 3 ML capped sample is due to expansion of {111} $SrTiO_3$ crystallographic planes in the vicinity of the interface, resulting from the expanded epitaxial $LaAlO_3$ layers in the ultrathin limit. Our results are important for improving superconducting devices from polar oxide interfaces.

VI. METHODS

A. Sample preparation

Sample Deposition. $LaAlO_3$ was deposited on atomically flat $SrTiO_3$ substrates using the pulsed laser deposition (PLD) technique following Ref. [37]. The deposition was monitored by reflection high-energy electron diffraction (RHEED). A successive layer of 10 nm of amorphous Al_2O_3 was deposited at room temperature *in situ* PLD using a sapphire single-crystal target, at oxygen pressure of 1.5 mTorr and laser fluence of $11.5\,mJ/mm^2$, or via *ex situ* atomic layer deposition (ALD) [44]. The results shown throughout this paper are independent of the Al_2O_3 deposition method.

TEM Sample Preparation. The 3 ML sample was prepared by a conventional cross-section method, including mechanical polishing using a MultiPrep^{TM} system (Allied High Tech, USA) followed by Ar ion milling using a PIPS II (Gatan, USA) apparatus at energies ranging from 4 down to 0.2 keV. To minimize damage induced by the ion milling, the sample was cooled to a temperature of 193 K. The 14 ML sample was prepared by a Ga^+ focused ion beam (FIB) Helios^{TM} 5 UC DualBeam (Thermo Fisher Scientific, USA) device employing the lift-out technique, using energies from 30 down to 2 keV. To protect the samples from ion beam damage, amorphous carbon and tungsten were deposited before the milling process.

B. Structural and compositional characterization

Structural characterization and compositional analysis were carried out using an aberration corrected scanning transmission electron microscope (STEM) Titan Themis G2 60-300 (Thermo Fisher Scientific, USA) operated at 300 keV and equipped with a Dual-X detector (Bruker, USA) having a collection solid angle of 1.76 srad. High-angle annular dark-field (HAADF) Z-contrast imaging with a drift-corrected frame integration function was used to characterize the crystal structures employing an angular collection range of 60–200 mrad and a beam diameter below 1 Å.

Energy-dispersive x-ray spectroscopy (EDS) was used to map and quantify elements based on the Sr L, Ti K, La L, and Al K characteristic energies; data analysis was carried out using Velox software (Thermo Fisher Scientific, USA). The elemental maps were prefiltered using 3 px average, background corrected using a multipolynomial fit (background order: 1 sloped), and postfiltered using Radial Wiener filter (highest frequency: 80, edge smoothing: 5). Concentration profiles were obtained by quantification without implementing absorption correction and postfiltering.

C. Strain analysis

Direct-space Analysis. Interplanar spacings were extracted from direct-space images using an algorithm in Python. The algorithm sums the HAADF STEM detector intensity in *y*- or *x*-directions of the image (in this work, [111] or [1$\bar{1}$0], respectively), forming a periodic signal that characterizes positions of crystallographic planes. Each peak obtained in the summed intensity plots is then fitted with a Gaussian, and the fitted peak positions are used to calculate adjacent interplanar spacings. See details in Sec. 6 of the Supplemental Material [29].

Geometric Phase Analysis. The strains within the samples were extracted from HAADF STEM images by the geometric phase analysis (GPA) [45] method using the Strain++ program [46], with reciprocal-lattice vectors $g_{1\bar{1}0}$ and g_{111} and a mask size of $1/2\,g_{1\bar{1}0}$.

D. Transport measurements

Hall Measurements. The Hall number was measured using a Keithley 6221 current source and a Keithley 2182A nanovoltmeter using a Quantum Design PPMS. The Hall number is inferred from the linear Hall resistivity measured in a Van-der-Pauw configuration, after averaging two contact configurations and antisymmetrizing with respect to the applied magnetic field.

Superconducting Properties. The superconducting properties were measured using a standard ac lock-in technique (Stanford SR830, frequencies in the range of 20–30 Hz) inside an Oxford Instruments Triton 400 dilution refrigerator. The critical temperature is defined as the temperature at which the resistance is half of the normal state resistance at 0.7 K.

ACKNOWLEDGMENTS

[1] J. F. Schooley, W. R. Hosler, and M. L. Cohen, Superconductivity in semiconducting SrTiO₃, Phys. Rev. Lett. **12**, 474 (1964).

[2] X. Lin, Z. Zhu, B. Fauqué, and K. Behnia, Fermi surface of the most dilute superconductor, Phys. Rev. X **3**, 021002 (2013).

[3] P. Wölfle and A. V. Balatsky, Superconductivity at low density near a ferroelectric quantum critical point: Doped SrTiO₃, Phys. Rev. B **98**, 104505 (2018).

[4] J. Ruhman and P. A. Lee, Comment on "superconductivity at low density near a ferroelectric quantum critical point: Doped SrTiO₃", Phys. Rev. B **100**, 226501 (2019).

[5] C. Collignon, X. Lin, C. W. Rischau, B. Fauqué, and K. Behnia, Metallicity and superconductivity in doped strontium titanate, Annu. Rev. Condens. Matter Phys. **10**, 25 (2019).

[6] M. N. Gastiasoro, J. Ruhman, and R. M. Fernandes, Superconductivity in dilute SrTiO₃: A review, Ann. Phys. **417**, 168107 (2020).

[7] C. S. Koonce, M. L. Cohen, J. F. Schooley, W. R. Hosler, and E. R. Pfeiffer, Superconducting transition temperatures of semiconducting SrTiO₃, Phys. Rev. **163**, 380 (1967).

[8] G. Binnig, A. Baratoff, H. E. Hoenig, and J. Q. Bednorz, Two-band superconductivity in Nb-doped SrTiO₃, Phys. Rev. Lett. **45**, 1352 (1980).

[9] M. Thiemann, M. H. Beutel, M. Dressel, N. R. Lee-Hone, D. M. Broun, E. Fillis-Tsirakis, H. Boschker, J. Mannhart, and M. Scheffler, Single-gap superconductivity and dome of superfluid density in Nb-doped SrTiO₃, Phys. Rev. Lett. **120**, 237002 (2018).

[10] B. Fauqué, C. Collignon, H. Yoon, Ravi, X. Lin, I. I. Mazin, H. Y. Hwang, and K. Behnia, Electronic band sculpted by oxygen vacancies and indispensable for dilute superconductivity, Phys. Rev. Res. **5**, 033080 (2023).

[11] A. D. Caviglia, Electric field control of the LaAlO₃/SrTiO₃ interface ground state, Nature (London) **456**, 624 (2008).

[12] E. Maniv, Strong correlations elucidate the electronic structure and phase diagram of LaAlO₃/SrTiO₃ interface, Nat. Commun. **6**, 8239 (2015).

[13] X. Lin, G. Bridoux, A. Gourgout, G. Seyfarth, S. Kramer, M. Nardone, B. Fauque, and K. Behnia, Critical doping for the onset of a two-band superconducting ground state in SrTiO₃₋δ, Phys. Rev. Lett. **112**, 207002 (2014).

[14] S. Gariglio, M. Gabay, and J. M. Triscone, Research update: Conductivity and beyond at the LaAlO₃/SrTiO₃ interface, APL Mater. **4**, 060701 (2016).

[15] C. Cancellieri, Electrostriction at the LaAlO₃/SrTiO₃ interface, Phys. Rev. Lett. **107**, 056102 (2011).

[16] F. W. Lytle, X-ray diffractometry of low-temperature phase transformations in strontium titanate, J. Appl. Phys. **35**, 2212 (1964).

[17] S. Thiel, G. Hammerl, A. Schmehl, C. W. Schneider, and J. Mannhart, Tunable quasi-two-dimensional electron gases in oxide heterostructures, Science **313**, 1942 (2006).

[18] M. Basletic, Mapping the spatial distribution of charge carriers in LaAlO₃/SrTiO₃ heterostructures, Nat. Mater. **7**, 621 (2008).

[19] Y. Yamada, H. K. Sato, Y. Hikita, H. Y. Hwang, and Y. Kanemitsu, Spatial density profile of electrons near the LaAlO₃/SrTiO₃ heterointerface revealed by time-resolved photoluminescence spectroscopy, Appl. Phys. Lett. **104**, 151907 (2014).

[20] T. T. Fister, Octahedral rotations in strained LaAlO₃/SrTiO₃ (001) heterostructures, APL Mater. **2**, 021102 (2014).

[21] A. Ohtomo and H. Y. Hwang, A high-mobility electron gas at the LaAlO₃/SrTiO₃ heterointerface, Nature (London) **427**, 423 (2004).

[22] R. Pentcheva and W. E. Pickett, Avoiding the polarization catastrophe in LaAlO₃ overlayers on SrTiO₃(001) through polar distortion, Phys. Rev. Lett. **102**, 107602 (2009).

[23] L. Yu and A. Zunger, A polarity-induced defect mechanism for conductivity and magnetism at polar–nonpolar oxide interfaces, Nat. Commun. **5**, 5118 (2014).

[24] E. Lesne, Suppression of the critical thickness threshold for conductivity at the LaAlO₃/SrTiO₃ interface, Nat. Commun. **5**, 4291 (2014).

[25] D. C. Vaz, Tuning up or down the critical thickness in LaAlO₃/SrTiO₃ through in situ deposition of metal overlayers, Adv. Mater. **29**, 1700486 (2017).

[26] R. S. Bisht, M. Mograbi, P. K. Rout, G. Tuvia, Y. Dagan, H. Yoon, A. G. Swartz, H. Y. Hwang, L. L. Li, and R. Pentcheva, Concomitant appearance of conductivity and superconductivity in (111) LaAlO₃/SrTiO₃ interface with metal capping, Phys. Rev. Mater. **6**, 044802 (2022).

[27] A. K. Singh, T. C. Wu, M. C. Chen, M. Y. Song, W. L. Lee, C. P. Su, and M.-W. Chu, Influence of SrTiO₃ capping layer on the charge transport at the interfaces of SrTiO₃/LaAlO₃/SrTiO₃ (100) heterostructure, Phys. Rev. Mater. **2**, 114009 (2018).

[28] Y. Kwak, Non-BCS-type superconductivity and critical thickness of SrTiO₃/LaAlO₃/SrTiO₃ trilayer interface system, Appl. Surf. Sci. **565**, 150495 (2021).

[29] See Supplemental Material at http://link.aps.org/supplemental/10.1103/PhysRevMaterials.8.084803 for other samples fabricated in this work, properties of the capped (100) interfaces, Hall measurements, evaluation of interplanar spacing, strain analysis, and further data regarding the uncapped 14 ML sample.

[30] N. Nakagawa, H. Y. Hwang, and D. A. Muller, Why some interfaces cannot be sharp, Nat. Mater. **5**, 204 (2006).

[31] P. R. Willmott, Structural basis for the conducting interface between LaAlO₃ and SrTiO₃, Phys. Rev. Lett. **99**, 155502 (2007).

[32] J. Liu, C. J. Barbero, J. W. Corbett, K. Rajan, and H. Leary, An in situ transmission electron microscopy study of electron-beam-induced amorphous-to-crystalline transformation of Al₂O₃ films on silicon, J. Appl. Phys. **73**, 5272 (1993).

[33] G. Herranz, F. Sánchez, N. Dix, M. Scigaj, and J. Fontcuberta, High mobility conduction at (110) and (111) LaAlO₃/SrTiO₃ interfaces, Sci. Rep. **2**, 758 (2012).

[34] S. Ryu, Electronic reconstruction at the polar (111)-oriented oxide interface, APL Mater. **10**, 031115 (2022).

[35] J. Cho and H. Jeen, Capping layers and their roles in polar catastrophe scenario of LaAlO₃/SrTiO₃(001) systems, J. Korean Phys. Soc. **81**, 984 (2022).

[36] M. Mograbi, E. Maniv, P. K. Rout, D. Graf, J. H. Park, and Y. Dagan, Vortex excitations in the insulating state of an oxide interface, Phys. Rev. B **99**, 094507 (2019).

[37] P. K. Rout, I. Agireen, E. Maniv, M. Goldstein, and Y. Dagan, Six-fold crystalline anisotropic magnetoresistance in the (111) LaAlO₃/SrTiO₃ oxide interface, Phys. Rev. B **95**, 241107(R) (2017).

[38] K. Ahadi, Enhancing superconductivity in SrTiO$_3$ films with strain, Sci. Adv. **5**, eaaw0120 (2019).

[39] C. Herrera, J. Cerbin, A. Jayakody, K. Dunnett, A. V. Balatsky, and I. Sochnikov, Strain-engineered interaction of quantum polar and superconducting phases, Phys. Rev. Mater. **3**, 124801 (2019).

[40] S. Hameed, Enhanced superconductivity and ferroelectric quantum criticality in plastically deformed strontium titanate, Nat. Mater. **21**, 54 (2021).

[41] J. Franklin, B. Xu, D. Davino, A. Mahabir, A. V. Balatsky, U. Aschauer, and I. Sochnikov, Giant Grüneisen parameter in a superconducting quantum paraelectric, Phys. Rev. B **103**, 214511 (2021).

[42] C. W. Bark, Tailoring a two-dimensional electron gas at the LaAlO$_3$/SrTiO$_3$ (001) interface by epitaxial strain, Proc. Natl. Acad. Sci. USA **108**, 4720 (2011).

[43] Z. Huang, Biaxial strain-induced transport property changes in atomically tailored SrTiO$_3$-based systems, Phys. Rev. B **90**, 125156 (2014).

[44] D. Miron, I. Krylov, M. Baskin, E. Yalon, and L. Kornblum, Understanding leakage currents through Al$_2$O$_3$ on SrTiO$_3$, J. Appl. Phys. **126**, 185301 (2019).

[45] M. J. Hÿtch, E. Snoeck, and R. Kilaas, Quantitative measurement of displacement and strain fields from hrem micrographs, Ultramicroscopy **74**, 131 (1998).

[46] J. Peters, Strain++ (2024), https://jjppeters.github.io/Strainpp/.